Oxygen reduction to water operating through the Direct (or Dissociative) Route: Descriptive and fitting capabilities of polarization curves

Mauricio D. Arce[1], José L. Fernández[*],[1]

Programa de Electroquímica Aplicada e Ingeniería Electroquímica (PRELINE), Facultad de Ingeniería Química, Universidad Nacional del Litoral. Santiago del Estero 2829 (S3000AOM) Santa Fe (Santa Fe) Argentina

ARTICLE INFO

ABSTRACT

The 4-e$^-$ oxygen reduction reaction (*orr*) to water operating through the Direct Route (dissociative chemical adsorption of molecular oxygen followed by a two-step electro-reduction of adsorbed atomic oxygen) in acid media was fully analyzed. An analytical equation for the dependence of the current density (j) on the overpotential (η) was derived in terms of the elementary kinetic constants and the adsorption parameters without aprioristic assumptions. The descriptive capability of this equation was thoroughly explored by simulations over wide ranges of these kinetic and adsorption parameters. It was demonstrated that the Direct Route predicts the existence of a maximum current density (j_{max}) that convolutes kinetic and mass-transport contributions. The value of j_{max} may approach the mass-transport limiting current density (j_L), although it will be smaller than this value when the rate of oxygen adsorption is small, and/or when j_L is very large. The application of Tafel plots for the analysis of the *orr* kinetics is contrasted to the rigorous equation derived in this work for this mechanistic route. The model was used to successfully correlate experimental $j(\eta)$ dependencies measured on Pt electrodes, and the obtained kinetic parameters were scrutinized.

© 2015 Elsevier Ltd. All rights reserved.

1. INTRODUCTION

The mechanism and kinetic parameters of the oxygen electrode reaction (*orr*) to water in acid media (defined by Eq. ((1)) on metal electrodes still are current topics under intense discussion, as evidenced by the continuous emergence of new reports with kinetic studies of this reaction over the last decade [1–13]. The importance of this reaction in Electrochemistry is primarily caused by its direct implications in energy storage/conversion devices (i.e. fuel cells) and in corrosion processes [14].

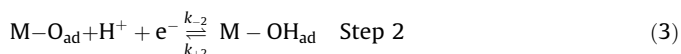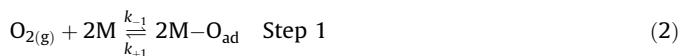$$O_{2(g)} + 4H^+ + 4e^- \rightarrow 2H_2O \tag{1}$$

The *orr* mechanism by itself is undoubtedly extremely complex since it must involve the transfer of four electrons and four protons, in addition to the O—O bond scission. This promotes the participation of a large number of adsorbed intermediates and elementary steps, with the consequent increment of possible reaction routes and secondary reactions such as metal electro-

oxidation [10] and hydrogen peroxide production [15]. Besides, the reaction rate is deeply affected by adsorption of anions [1]. Experimental and theoretical studies helped to clarify many aspects of the involved mechanistic steps, and nowadays there is a well accepted mechanistic scheme. This scheme, which was initially proposed by Wroblowa et al. [16] and later refined by other researchers [17,18], involves the possible participation of two parallel routes or pathways for the 4e$^-$-reduction of the oxygen molecule. These routes are known as the Direct (or Dissociative) and the Serial (or Associative) Pathways [18]. While the adsorption of an oxygen molecule in the first one occurs through a dissociative chemical step (generating two O$_{ad}$ intermediates), in the second one it proceeds through an electrochemical step involving a single electron and proton transfer (generating one OOH$_{ad}$ intermediate). Which one of these routes should prevail at each potential still is a controversial issue even on platinum, the most studied material [5,6,8,12]. On the basis of hydrogen peroxide yields and DFT calculations, it is believed that the occurrence of the *orr* through the dissociative chimisorption of oxygen is unfavorable against the electrochemical adsorption [19], but issues related with the experimental polarization curves (mainly Tafel slopes and reaction orders) still need to be explained [6].

---

[*] Corresponding author. Tel.: +54 342 4571164 Ext. 2519.
E-mail address: jlfernan@fiq.unl.edu.ar (J.L. Fernández).
[1] ISE member.

In particular, the Direct Route takes place through the three elementary steps indicated by Eqs. (2)–(4) (where M specifies a metal active site), that involve the dissociative chemical adsorption of the oxygen molecule generating two atomic oxygen intermediates (O_{ad}), followed by their electro-reduction to OH_{ad} and finally H_2O [18].

$$O_{2(g)} + 2M \underset{k_{+1}}{\overset{k_{-1}}{\rightleftharpoons}} 2M-O_{ad} \quad \text{Step 1} \tag{2}$$

$$M-O_{ad} + H^+ + e^- \underset{k_{+2}}{\overset{k_{-2}}{\rightleftharpoons}} M-OH_{ad} \quad \text{Step 2} \tag{3}$$

$$M-OH_{ad} + H^+ + e^- \underset{k_{+3}}{\overset{k_{-3}}{\rightleftharpoons}} H_2O \quad \text{Step 3} \tag{4}$$

This sequence of steps is the simplest way that can be followed to electro-reduce the oxygen molecule to water [18]. Thus, taking into account that the dependencies of the current density (j) on the overpotential (η) are still the most used experimental evidences to inspect the mechanisms of electrode reactions and to obtain the kinetic parameters, it is important to aprioristically know the possible $j(\eta)$ scenarios that the proposed mechanism would be able to describe.

As the *orr* requires the dissolution of $O_{2(g)}$ and the transport of $O_{2(dis)}$ to the electrode surface, and due to the low solubility of $O_{2(dis)}$ in most aqueous media, the mass transport conditions play an important role in the $j(\eta)$ response over the whole range of η [2]. To separate from the experimental $j(\eta)$ dependence the mass-transport contribution and the apparently pure kinetic contribution (i.e. the so-called kinetic current density, j_k), it is usual to apply the Koutecký–Levich (KL) formalism [20] leading to the well-known Tafel plots, or $j_k(\eta)$ dependencies. However, it should be kept in mind that the KL equation was derived for a totally irreversible one-step and one-electron reaction [21]. Such over-simplified hypothesis is not compatible with the complex mechanism of the *orr*, even for the simplest case where it operates through the Direct Route. Thus, the KL treatment may not be capable to reproduce the complete $j(\eta)$ dependence of the *orr* over the complete η range, and the obtained $j_k(\eta)$ dependencies may not necessarily correspond to a purely kinetically controlled response.

In this context, this work analyzes the expected $j(\eta)$ dependencies that should result when the Direct Route is the only operative route during the *orr*, by treating this mechanism in a complete and rigorous way without pre-assumptions about rate-determining steps. The effect of the elementary kinetic parameters on the $j(\eta)$ curves are explored by simulations, aiming mainly to evaluate whether the descriptive capability of the equation allows to describe the main experimental features of the $j(\eta)$ dependencies reported so far for Pt and other noble metals. The application of KL and Tafel-plot based treatments on selected simulated curves is critically discussed. Moreover, the model was used to correlate experimental $j(\eta)$ data, both measured in this work and reported in the literature on Pt microelectrodes and rotating disk electrodes.

2. THEORY

2.1. The complete j(η) dependence

The rate of the *orr* (v) can be related to the rates of the elementary steps (v_i, where the subscript i is the step number given in Eqs. ((2)–(4)) through a mass balance in steady state, which results in the equivalences given by Eq. (5).

$$v = v_1 = \frac{1}{2}v_2 = \frac{1}{2}v_3 \tag{5}$$

The Absolute Rate Theory [22] allows to describe the elementary step rates in terms of η, the kinetic parameters, the activities of dissolved species (a_i) at the surface, the fugacity of O_2 (f_{O2}) at the surface, and the surface coverage of adsorbed intermediates (θ_i). Besides, the behavior of adsorbed species can be described through the Frumkin isotherm [23]. Thus, by approximating the activities to the molar concentrations ($a_i \cong C_i$), and taking into account that $f_{O2} \cong K_{O2}C_{O2}$ (where K_{O2} is the Henry constant), the elementary step rates result according to Eqs. (6)–(8).

$$\begin{aligned} v_1 &= v_{-1} - v_{+1} \\ &= v_1^e e^{-2\lambda u_1(\theta - \theta^e)} \left[\left(\frac{1-\theta}{1-\theta^e} \right)^2 c_{O_2}^s - \left(\frac{\theta_1}{\theta_1^e} \right)^2 e^{-2u_1(\theta - \theta^e)} \right] \end{aligned} \tag{6}$$

$$\begin{aligned} v_2 &= v_{-2} - v_{+2} \\ &= v_2^e e^{-\lambda(u_1 - u_2)(\theta - \theta^e)} e^{-\alpha f \eta} \left[\left(\frac{\theta_1}{\theta_1^e} \right) e^{(u_1 - u_2)(\theta - \theta^e)} c_{H^+}^s - \left(\frac{\theta_2}{\theta_2^e} \right) e^{f\eta} \right] \end{aligned} \tag{7}$$

$$\begin{aligned} v_3 &= v_{-3} - v_{+3} \\ &= v_3^e e^{-\lambda u_2(\theta - \theta^e)} e^{-\alpha f \eta} \left[\left(\frac{\theta_2}{\theta_2^e} \right) e^{u_2(\theta - \theta^e)} c_{H^+}^s - \left(\frac{1-\theta}{1-\theta^e} \right) e^{f\eta} \right] \end{aligned} \tag{8}$$

The coverages θ_1 and θ_2 refer to the adsorbed intermediates O_{ad} and OH_{ad}, respectively, while $\theta = \theta_1 + \theta_2$ (thus $1 - \theta$ represents the free metal sites, as the adsorption of anions was not considered in this model). The superscripts "e" and "s" indicate the values of the variable at the equilibrium potential of the *orr* and at the electrode surface, respectively. Besides, α is the symmetry factor of the electrochemical steps (considered identical for both steps), $c_i^s = C_i^s / C_i^e$, and $f = F/RT$. The Frumkin isotherm involves the interaction parameters of each adsorbed species (u_i, in RT units), and the symmetry factor of the adsorption processes (λ) [23]. It should be remarked that the specific rate constants of each elementary step ($k_{\pm i}$) are involved in these equations through the equilibrium rates (v_i^e, in mol s^{-1} cm^{-2}), which are defined according to Eqs. (9)–(11).

$$v_1^e = k_{-1}(1 - \theta^e)^2 f_{O_2} e^{-2\lambda u_1 \theta^e} = k_{+1}\theta_1^{e2} e^{2(1-\lambda)u_1 \theta^e} \tag{9}$$

$$v_2^e = k_{-2}\theta_1^e e^{(1-\lambda)(u_1 - u_2)\theta^e} C_{H^+}^e e^{-\alpha f E^e} = k_{+2}\theta_2^e e^{-\lambda(u_1 - u_2)\theta^e} e^{(1-\alpha)f E^e} \tag{10}$$

$$v_3^e = k_{-3}\theta_2^e e^{(1-\lambda)u_2 \theta^e} C_{H^+}^e e^{-\alpha f E^e} = k_{+3}(1 - \theta^e)e^{-\lambda u_2 \theta^e} e^{(1-\alpha)f E^e} \tag{11}$$

In strong acid media, the surface concentration of H^+ can be considered almost invariant ($c_{H^+}^s \cong 1$). Moreover, the surface concentration of dissolved O_2 can be related to the mass transport liming current density (j_L) by assuming a linear diffusion layer approximation, on which $c_{O_2}^s = 1 - j/j_L$. This is a good approximation for electrode configurations that define a planar diffusion layer, such as the rotating disk electrode. Moreover, for the sake of simplicity this model is also frequently used to arrive to analytical expressions that allow to treat complex mechanisms operating under mixed control on electrode geometries that define radial diffusion (such as spherical, disk and ring microelectrodes [24,25]. Thus, by combining Eqs. (5)–(8) and taking into account that $j = 4Fv$, the dependencies $j(\eta, \theta_1(\eta), \theta_2(\eta))$ given by Eq. (12) are obtained.

$$j = \frac{\left(\frac{1-\theta}{1-\theta^e}\right)^2 - \left(\frac{\theta_1}{\theta_1^e}\right)^2 e^{2u_1(\theta-\theta^e)}}{\frac{e^{2\lambda u_1(\theta-\theta^e)}}{4Fv_1^e} + \left(\frac{1-\theta}{1-\theta^e}\right)^2 \frac{1}{j_L}} =$$

$$= 2Fv_2^e e^{-\lambda(u_1-u_2)(\theta-\theta^e)} e^{-\alpha f\eta}\left[\left(\frac{\theta_1}{\theta_1^e}\right)e^{(u_1-u_2)(\theta-\theta^e)} - \left(\frac{\theta_2}{\theta_2^e}\right)e^{f\eta}\right] =$$

$$= 2Fv_3^e e^{-\lambda u_2(\theta-\theta^e)} e^{-\alpha f\eta}\left[\left(\frac{\theta_2}{\theta_2^e}\right)e^{u_2(\theta-\theta^e)} - \left(\frac{1-\theta}{1-\theta^e}\right)e^{f\eta}\right] \quad (12)$$

It should be noted that the $\theta_1(\eta)$ and $\theta_2(\eta)$ dependencies can be obtained for a given set of kinetic parameters by solving the second and third equalities of Eq. (12).

2.2. Limiting conditions

2.2.1. Maximum current density

An interesting property of the $j(\eta)$ dependence previously obtained for the Direct Route is its limiting behavior when $\eta \to -\infty$, where it is verified that $\theta_1 \to 0$ and $\theta_2 \to 0$. By applying this condition to Eq. (12), a maximum value of j (j_{max}) independent of η is reached, which is given by Eq. (13).

$$j_{max} = \lim_{\eta \to -\infty}(j) = \frac{1}{\frac{(1-\theta^e)^2 e^{-2\lambda u_1 \theta^e}}{4Fv_1^e} + \frac{1}{j_L}} \quad (13)$$

This maximum current density convolutes diffusional (through j_L) and kinetic contributions. This observation is important since it points out that, depending on the relative values of both terms involved in the denominator of Eq. (13), the j_{max} value could be quite smaller than the j_L value. More precisely, if j_L is much smaller than the value of the term $4Fv_1^e/(1-\theta^e)^2$, then j_{max} is essentially identical to j_L. However, when that condition is not fulfilled, for example because v_1^e is very small (when the dissociative adsorption of oxygen is slow) or j_L is very large (in conditions of high mass transport rates), then j_{max} will be smaller than j_L. This phenomenon occurs because a slow chemical step (even slower than the speed of mass transport) ends up governing the rate of the overall electrochemical reaction, which becomes independent of the applied potential. Besides, under these conditions the surface concentration of dissolved oxygen does not fall to zero for $\eta \to -\infty$.

2.2.2. Activated current density

The activated current density (j_{act}) can be obtained in the limiting condition where the mass transport rate is infinite, and represents the current density free of mass transport effects. This situation implies that $j_L \to \infty$ and $c_{O2}^s = 1$. Thus, by applying these conditions either to Eq. (12) ($j_L \to \infty$) or to Eq. (5)–(8) ($c_{O2}^s = 1$), the $j_{act}(\eta)$ dependencies given by Eq. (14) are obtained, where θ_i^* are the coverages of intermediates resulting for activated conditions.

$$j_{act} = 4Fv_1^e e^{-2\lambda u_1(\theta^*-\theta^e)}\left[\left(\frac{1-\theta^*}{1-\theta^e}\right)^2 - \left(\frac{\theta_1^*}{\theta_1^e}\right)^2 e^{2u_1(\theta^*-\theta^e)}\right] =$$

$$= 2Fv_2^e e^{-\lambda(u_1-u_2)(\theta^*-\theta^e)} e^{-\alpha f\eta}\left[\left(\frac{\theta_1^*}{\theta_1^e}\right)e^{(u_1-u_2)(\theta^*-\theta^e)} - \left(\frac{\theta_2^*}{\theta_2^e}\right)e^{f\eta}\right] =$$

$$= 2Fv_3^e e^{-\lambda u_2(\theta^*-\theta^e)} e^{-\alpha f\eta}\left[\left(\frac{\theta_2^*}{\theta_2^e}\right)e^{u_2(\theta^*-\theta^e)} - \left(\frac{1-\theta^*}{1-\theta^e}\right)e^{f\eta}\right] \quad (14)$$

2.3. Application of Tafel plots

By applying the KL formalism to the complete $j(\eta)$ functionality given by Eq. (12), the dependence of the so-called kinetic current density (j_k) on η becomes defined by Eq. (15).

$$j_k = \left(\frac{1}{j} - \frac{1}{j_L}\right)^{-1} = \frac{\left(\frac{1-\theta}{1-\theta^e}\right)^2 e^{-2u_1(\theta-\theta^e)} - \left(\frac{\theta_1}{\theta_1^e}\right)^2}{\frac{e^{-2(1-\lambda)u_1(\theta-\theta^e)}}{4Fv_1^e} + \left(\frac{\theta_1}{\theta_1^e}\right)^2 \frac{1}{j_L}} =$$

$$= \left[\frac{1}{2Fv_2^e e^{-\lambda(u_1-u_2)(\theta-\theta^e)} e^{-\alpha f\eta}\left[\left(\frac{\theta_1}{\theta_1^e}\right)e^{(u_1-u_2)(\theta-\theta^e)} - \left(\frac{\theta_2}{\theta_2^e}\right)ef\eta\right]} - \frac{1}{j_L}\right]^{-1} =$$

$$= \left[\frac{1}{2Fv_3^e e^{-\lambda u_2(\theta-\theta^e)} e^{-\alpha f\eta}\left[\left(\frac{\theta_2}{\theta_2^e}\right)e^{u_2(\theta-\theta^e)} - \left(\frac{1-\theta}{1-\theta^e}\right)ef\eta\right]} - \frac{1}{j_L}\right]^{-1}$$

$$(15)$$

It is clear that for the Direct Route the variable j_k that results from the KL treatment is not independent of j_L and will only be representative of a pure kinetic behavior when some particular conditions apply over restricted potential intervals. Besides, it may be possible that linear regions in the logarithmic $j_k(\eta)$ dependence (Tafel plots) could be defined for certain conditions, and this will be discussed in a following section.

3. EXPERIMENTAL

3.1. Electrodes

Platinum disk microelectrodes with radii (r) in the range $1\,\mu m < r \le 12.5\,\mu m$ were fabricated by heat sealing of sharpened wires into borosilicate glass capillaries by a procedure previously described [26]. Platinum wires (25 μm diameter, Alpha Aesar) were electrochemically etched in solution of 4.5 M CaCl$_2$ in 1 M HCl, by applying an ac voltage (sine wave, 50 Hz, ± 2 V peak to peak) against a concentric annular Pt counter-electrode (5 mm opening). The etched wire with a sharp tip was then introduced into a borosilicate glass capillary (1 mm outer diameter, 0.1 mm thickness), which end was melted by careful heating under a torch flame until the sealing of about 2 mm of the etched wire was visually verified. The sealed capillary was polished with a sequence of fine sandpapers (down to 2500 grits) and with a polishing pad with alumina slurry until the exposure of the metal disk was detected. The quality and size of the microelectrodes were evaluated by optical microscopy and cyclic voltammetry in ferrocene methanol solution [27].

3.2. Electrochemical experiments

The *orr* was studied in 0.5 M H$_2$SO$_4$ solution (Merck) saturated with O$_2$ (>99.9 %) at 1 atm. Water used in all solutions was first deionized with an exchange resin, then doubly distilled, and finally treated with a Purelab purifier (Elga Labwater, resistivity ≥ 18.2 MΩ cm). All electrochemical measurements were performed using a PC-commanded potentiostat CHI-1140B (CH Instruments). A typical three-electrode cell was used, where the Pt microelectrode was the working electrode and a large-area Pt wire placed in the same vessel was the counter-electrode. The reference electrode

was a Reversible Hydrogen Electrode (RHE) prepared *in situ* in the same solution. Saturation of the solutions with O_2 was attained by bubbling the purified gas through a glass pipe with an airstone at its end placed concentric to a glass bell with holes, which allowed the circulation of the solution in intimate contact with the gas avoiding strong agitation of the bulk solution. Steady-state polarization curves for the *orr* were acquired point by point over the complete potential range every 0.025 V. A potential program including oxidation (1.0 V vs. RHE) and reduction (0.1 V vs. RHE) steps before each measuring step was used [26]. The quality and cleanliness of the Pt surface and solution was checked by cyclic voltammograms in N_2-saturated 0.5 M H_2SO_4 solution [28]. The real areas of the Pt microelectrodes were estimated from these cyclic voltammograms using the charge of upd-H adsorption [29], although these values resulted only slightly larger than the respective geometric areas calculated from the microelectrode sizes (roughness factors in the range 1.2–1.5). Thus, the geometric areas were used for calculation of current densities.

4. Results and discussion

4.1. Simulation of j(η) dependencies

The effects of the involved kinetic and adsorption parameters on the main features of the polarization curves were analyzed by performing simulations of the $j(\eta)$, $\theta_1(\eta)$ and $\theta_2(\eta)$ dependencies using Eq. (12). These calculations were carried out using the software Micromath Scientist 3.0. The independent kinetic parameters that are involved in these equations are v_1^e, v_2^e, v_3^e, θ_1^e, θ_2^e, u_1 and u_2. All the other kinetic constants (for example, the elementary rate constants $k_{\pm i}$ of the elementary steps) can be calculated from this set using Eqs. (9)-(11). An analysis covering all possible combinations of parameter values would be too lengthy. Thus, the effects of the v_i^e and u_i values were only analyzed for

cases where it is expected that the metal is almost fully covered with OH_{ad} at the equilibrium potential (i.e., $\theta_2^e \cong 1$ and $\theta_1^e \cong 0$).

The graphs that are shown in Fig. 1 present $j(\eta)$ curves simulated in conditions where the j_{max} value may substantially separate from the j_L value, and exemplify the effect that the different kinetic and mass transport parameters could have on this magnitude. As expected, an increase of j_L (Fig. 1A) causes a shift in the polarization curve and also a decrease of j_{max} for certain j_L values (depending on the relative weights of both terms in the denominator of Eq. ((13)). From Fig. 1B it is verified that for a fixed mass transport rate, a decrease of v_1^e only causes a drop of j_{max}, but does not affect the overpotential for the *orr*. It should be noted that for metals that are electro-oxidized at the equilibrium potential of the *orr* (such as Pt) it is expected that θ_2^e will be close to 1, and as a consequence, the term $(1 - \boldsymbol{\theta}^e)$ in the expression of j_{max} given by Eq. (13) will approach to 0. Such effect of θ_2^e on j_{max} is clearly seen in Fig. 1C, where it is verified that upon bringing the value of θ_2^e close to 1, the j_{max} value closely approaches to j_L. This should occur even for very large j_L values, unless v_1^e is extremely small. In fact, as the electro-oxidation potential of a metal through step 3 is directly associated to its free energy for dissociative adsorption of oxygen (step 1) [30], it is likely that a metal with low θ_2^e will also have a small v_1^e value. Thus, metals such as Pt or Pd that are known to be almost completely electro-oxidized at the reversible potential of the *orr*, will hardly define a j_{max} value different to j_L. On the other hand, a metal such as Au whose electro-oxidation potential is more anodic and that is a poor oxygen cleaver, will surely reach a very small j_{max} value, probably experimentally undetectable (which is supported by the proved inability of this metal to reduce oxygen directly to water in acidic media [31,32]. It should be mentioned that a kinetic limiting behavior for the *orr* was only detected on Pt in slightly alkaline solutions using scanning electrochemical microscopy [33] (in conditions of high mass transport rates).
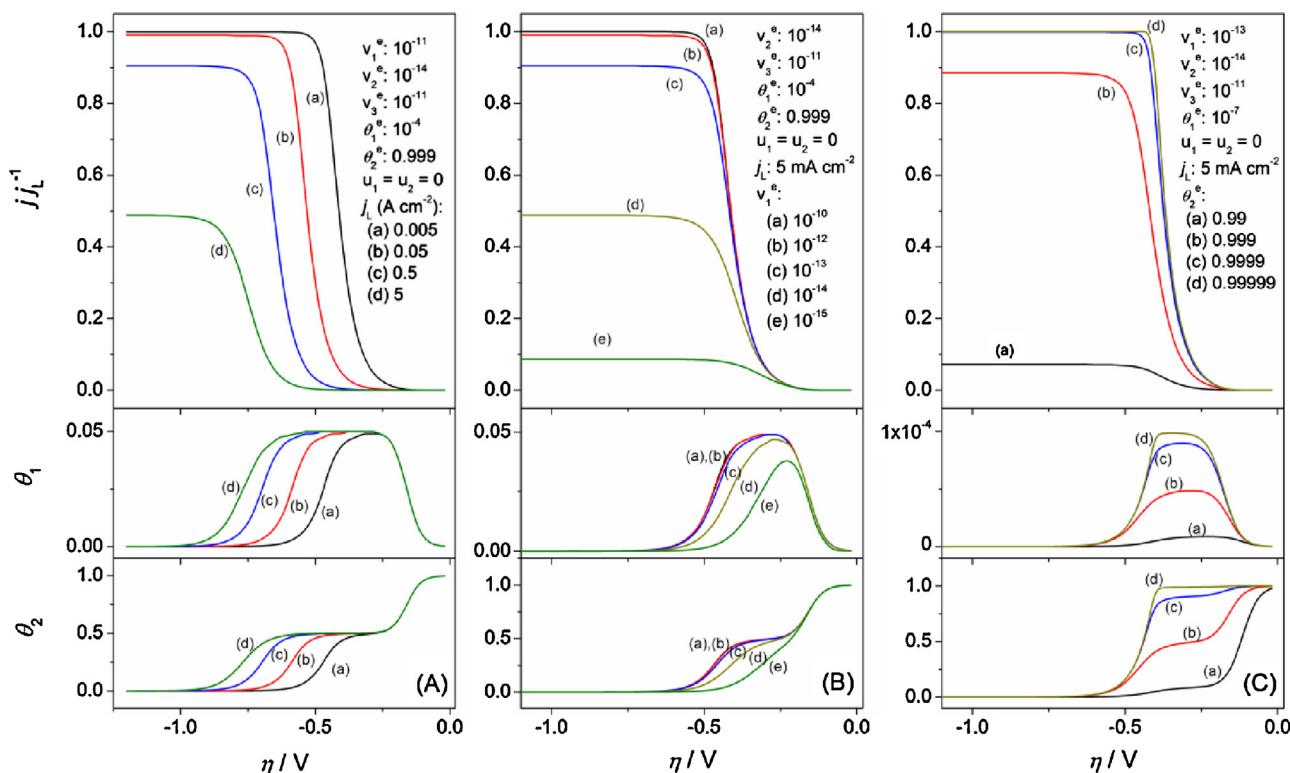
Fig. 1. Simulations of normalized $j(\eta)$, $\theta_1(\eta)$ y $\theta_2(\eta)$ dependencies for the *orr* operating through the Direct Route showing the effect of j_L (A), v_1^e (B) and θ_2^e (C) on j_{max}. Parameters are indicated within the graphs (v_i^e in mol s^{-1} cm^{-2}).

The dependencies $\theta_1(\eta)$ and $\theta_2(\eta)$ present at least three distinctive regions. The first region at low η values ($|\eta| < 0.2$ V) shows a decrease of θ_2 and simultaneous increase of θ_1 as η becomes more cathodic, variations that are independent of the mass-transport rate. This behavior is caused by the release of OH_{ad}-occupied sites through step 3 and simultaneous adsorption of O_{ad} through step 1. The second region is caused by the transformation of O_{ad} into OH_{ad} through step 2 (delayed by the low value of v_2^e) at a rate similar to the consumption of OH_{ad} through step 3, causing that both coverages reach invariant values over a limited η interval. However, as soon as the overpotential is high enough (third region) to drive the consumption of O_{ad} and OH_{ad} through steps 2 and 3 at a rate that cannot be followed by the reposition of O_{ad} through step 1, both coverages drop. The overpotential from which this process occurs is sensitive to the mass transport rate of dissolved oxygen, as it affects step 1. Besides, the observed plateaus in the $\theta_i(\eta)$ dependencies have extensions and magnitudes that depend on the relative values of the equilibrium rates.

The effect of the ratio v_3^e/v_2^e is illustrated in Fig. 2, which shows that when v_1^e is large the relative values of v_3^e and v_2^e control the $j(\eta)$ dependence and determine which of these two steps (if any) dominates the global reaction rate. Thus, it can be seen that for $v_3^e/v_2^e \geq 10^2$ the $j(\eta)$ dependence is mostly governed by step 2, while when $v_3^e/v_2^e \leq 10^{-1}$ the curve is controlled by step 3. In the range $10^{-1} \leq v_3^e/v_2^e \leq 10^2$ both steps contribute to the $j(\eta)$ dependence.

It should be noted that when step 2 limits the reaction rate (i.e. curves (a) in Fig. 2) the coverage of OH_{ad} decreases to small values at low overpotentials and the O_{ad} intermediate accumulates (increasing its coverage) until η is sufficiently large to increase the rate of step 2 converting all O_{ad} into OH_{ad}, followed by its immediate reduction to water (as step 3 is fast). On the other hand, when step 3 limits the reaction rate (i.e. curves (d) and (e) in Fig. 2)
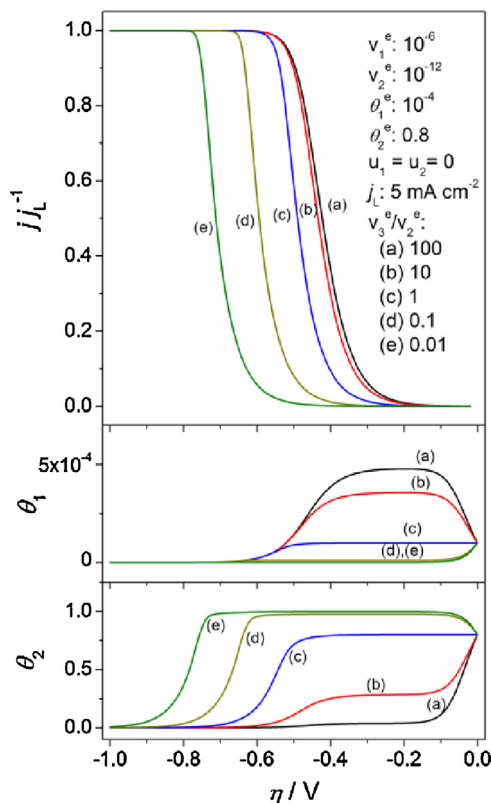
θ_2 increases to near 1 and the electrode surface remains almost fully covered by OH_{ad} down to very large η values, delaying the increase of the electrode current to those overpotentials. In the transitional situations where neither step 2 nor step 3 are limiting steps, the coverage of OH_{ad} decreases at low overpotential reaching the previously mentioned plateau (which value in this case depends on v_3^e) that is maintained over a η range whose extension is also affected by the value of v_2^e.
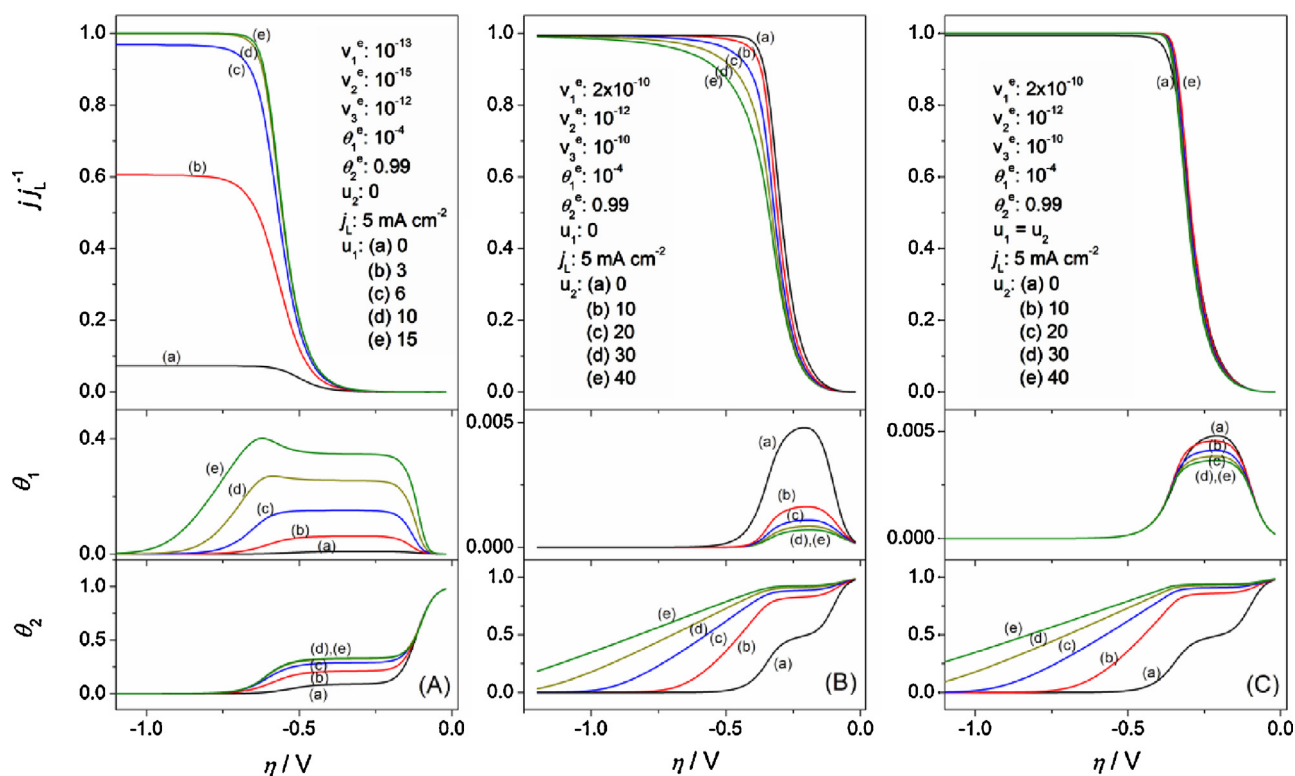
As it is known that the behavior of the adsorbed species may have critical effects on the $j(\eta)$ dependencies [1,10], the Frumkin interaction parameters were varied even over positive ranges that exceed the usually accepted values. Some of the resulting curves for varying u_1 and u_2 values are shown in Fig. 3.

On the one hand, in Fig. 3A the effect of only u_1 is observed (assuming no interactions of OH_{ad}, or $u_2 = 0$). In these conditions u_1 mainly affects the value of j_{max}, which is expected from Eq. (13), and the $\theta_1(\eta)$ dependence. On the other hand, the effect of u_2 is seen in Fig. 3B (assuming no interactions of O_{ad}, or $u_1 = 0$), which shows that an increase of u_2 causes a significant change in the slope of the $j(\eta)$ dependence, particularly for the unusually large u_2 values. This is concomitant with a slower consumption of OH_{ad} upon increasing the overpotential, (which is evidenced by a decrease in the slope of the $\theta_2(\eta)$ dependence and an increase of the θ_2 plateau value) and with a decrease in the O_{ad} coverage. In fact, Fig. 3C shows that if $u_1 = u_2$, the effect of u_2 on $j(\eta)$ and on $\theta_1(\eta)$ that was observed in Fig. 3B is no longer effective (although the behavior of the $\theta_i(\eta)$ and $j(\eta)$ dependences are quite similar to this case), pointing that what causes the slope change in the $j(\eta)$ dependence is the inequality between both parameters.

Finally, the effect of θ_2^e and θ_1^e can be seen in Fig. 4. A variation of the equilibrium coverage of OH_{ad} causes very different effects depending on the relative values of v_2^e and v_3^e. In the cases where v_3^e is small (Fig. 4A), a decrease of θ_2^e shifts the $j(\eta)$ curves to lower η values. Due to the low v_3^e, the reduction of OH_{ad} to water through step 3 is relegated to more cathodic potentials, causing an increment of θ_2 through step 2 as η increases in the domain of low η, so that θ_2/θ_2^e is always larger than 1. Thus, for decreasing θ_2^e values the term θ_2/θ_2^e becomes larger, increasing the rate of step 3 (and so the global reaction rate) at each overpotential (see Eq. (8)), causing the shift of the $j(\eta)$ curves to lower η. On the contrary, Fig. 4B shows that when v_2^e is small, the $j(\eta)$ curve shifts to smaller η values as θ_2^e becomes larger. In this condition θ_2 always decreases through step 3 as η increases, and $(1 - \boldsymbol{\theta})$ tends to 1. Thus, for θ_2^e values close to 1 (or $1 - \boldsymbol{\theta}^e$ almost null), the rate of step 1 (and of the global reaction) at a certain η value is increased due to an increase of the term $(1 - \theta)^2/(1 - \boldsymbol{\theta}^e)^2$ (see Eq. (6)) leading to the observed $j(\eta)$ shift. This effect could also be visualized in the first equality of Eq. (12), where $(1 - \boldsymbol{\theta}^e)^2$ multiplies j_L. Thus, an increase of θ_2^e (decrease of $1 - \boldsymbol{\theta}^e$) would produce a net effect similar to reducing j_L (shifting of the $j(\eta)$ curve to lower η). In both cases, an effect on j_{max} is also observed as θ^e becomes too small, as already shown in Fig. 1C. On the other hand, the situation presented in Fig. 4C shows that an increase of θ_1^e from very low values to near 1, without changing θ_2^e, only produces an increase of j_{max} (for $\theta_1^e > 0.9$, $j_{max} \cong j_L$).

4.2. KL treatment and Tafel plots of simulated $j(\eta)$ dependencies

The KL method is nowadays the most accepted procedure for the analysis of experimental $j(\eta)$ dependencies measured on electrode reactions that operate under mixed conditions. The method was originally conceived [20] as a tool to separate the pure mass transport contribution (through j_L) from the pure kinetic response (j_k) in irreversible single step reactions that are first order with respect to the reactant [21] through the simple relationship $1/j_k(\eta) = 1/j(\eta) - 1/j_L$. Its great simplicity propitiated its application to


Fig. 2. Simulations of normalized $j(\eta)$, $\theta_1(\eta)$ y $\theta_2(\eta)$ dependencies for the *orr* operating through the Direct Route showing the effect of v_2^e and v_3^e. Parameters are indicated within the graphs (v_i^e in mol s^{-1} cm^{-2}).

Plot legend values:
v_1^e: 10^{-6}
v_2^e: 10^{-12}
θ_1^e: 10^{-4}
θ_2^e: 0.8
$u_1 = u_2 = 0$
j_L: 5 mA cm^{-2}
v_3^e/v_2^e:
(a) 100
(b) 10
(c) 1
(d) 0.1
(e) 0.01

Fig. 3. Simulations of normalized $j(\eta)$, $\theta_1(\eta)$ y $\theta_2(\eta)$ dependencies for the *orr* operating through the Direct Route showing the effect of u_1 (A), u_2 (B), and of $u_1 = u_2$ (C). Parameters are indicated within the graphs (v_i^e in mol s^{-1} cm^{-2}).
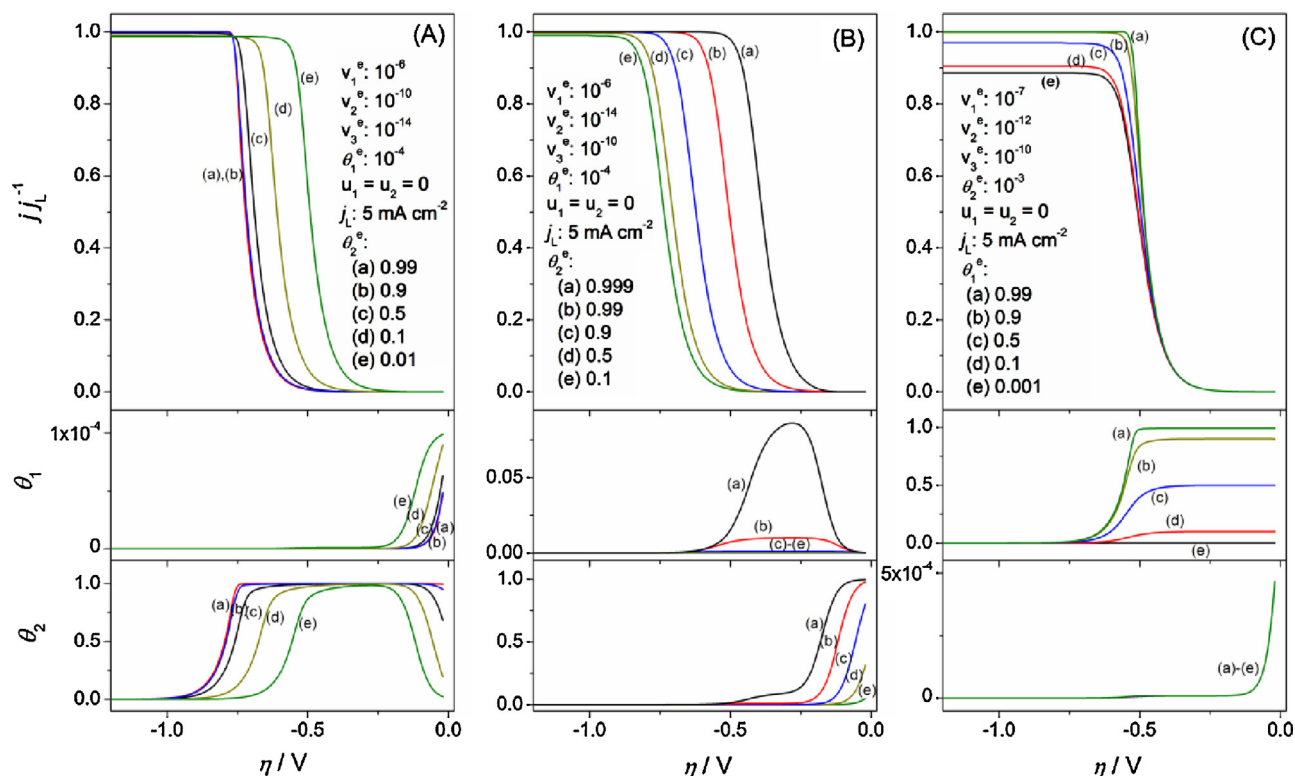
Fig. 4. Simulations of normalized $j(\eta)$, $\theta_1(\eta)$ y $\theta_2(\eta)$ dependencies for the *orr* operating through the Direct Route showing the effect of θ_2^e(A and B) and θ_1^e (C). Parameters are indicated within the graphs (v_i^e in mol s^{-1} cm^{-2}).

more complex multistep reactions, including the *orr* [34], although in most cases its validity is not guaranteed as the required

conditions are not necessarily accomplished. In fact, it was demonstrated in the Theory section that even in the simplest
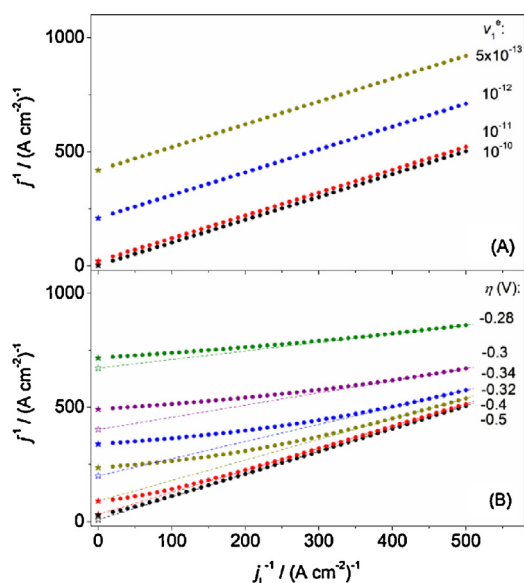
Fig. 5. Simulated j^{-1} vs. j_L^{-1} curves for application of the Koutecký–Levich method. (A) Kinetic parameters as in Fig. 1A for different values of v_1^e (in mol s^{-1} cm^{-2}) indicated within the graph and $\eta = -1.2$ V. (B) Kinetic parameters as in Fig. 3B and $u_2 = 20$, for different values of η indicated within the graph. Dashed lines are linear fittings of the simulated dependencies over apparently linear ranges. Star symbols indicate the $j_{act}(\eta)$ values calculated with Eq. (14) (solid stars) and the $j_k(\eta)$ values (open stars).

orr mechanism (the Direct Route) there is no reason to think that the j_k value obtained by the KL method (Eq. (15)) will be identical to the activated value (j_{act}) free of mass transport effects (Eq. (14)).

In general, the application of the KL method to extract j_k may follow two procedures. In those cases where the electrode configuration allows to easily change the mass transport rate, such as hydrodynamic electrodes (i.e. the rotating disk electrode, where j_L is proportional to the square root of the rotation rate, ω), it is usual to obtain j_k from the extrapolation of an apparently linear region of the $j^{-1}(j_L^{-1})$ dependence at varied overpotentials [34]. When applying this procedure to the *orr* operating through the Direct Route two issues should be remarked. On the one hand at large values of η, while in a single electrode reaction the value of j tends to j_L, in the Direct Route the value of j tends to j_{max}, which in fact depends on j_L according to Eq. (13). Thus, as it is exemplified in Fig. 5A, the ordinate of the linear $j^{-1}(j_L^{-1})$ dependence is the inverse of the activated maximum current density, which strictly is a finite value that will only approach to zero when $j_{max} \cong j_L$ depending on the values of v_1^e, θ^e and u_1.

On the other hand, for lower overpotentials the values of j_k at each η can be obtained from the extrapolation of a linear region of the $j^{-1}(j_L^{-1})$ dependence, as it is shown in Fig. 5B. However, it is seen that these extrapolated j_k values may be quite different to the real j_{act} values calculated with Eq. (14). Thus, as it is observed in Fig. 6A, the resulting Tafel plots (j_k vs. η) deviates significantly from the actual pure kinetic response (j_{act} vs. η).

The second common KL procedure to obtain Tafel plots from experimental $j(\eta)$ data relies on the calculation of the $j_k(\eta)$ dependence directly from the relationship $1/j_k(\eta) = 1/j(\eta) - 1/j_L$ at each overpotential. This procedure is mostly used when the mass transport rate cannot be straightforwardly changed on a single electrode, for example in microelectrodes or in other electrode configurations where the mass transport conditions are defined by the electrode geometry. When this method is applied to the simulated $j(\eta)$ curves that are derived from the Direct Route, the resulting $j_k(\eta)$ dependencies still remain dependent on j_L and do
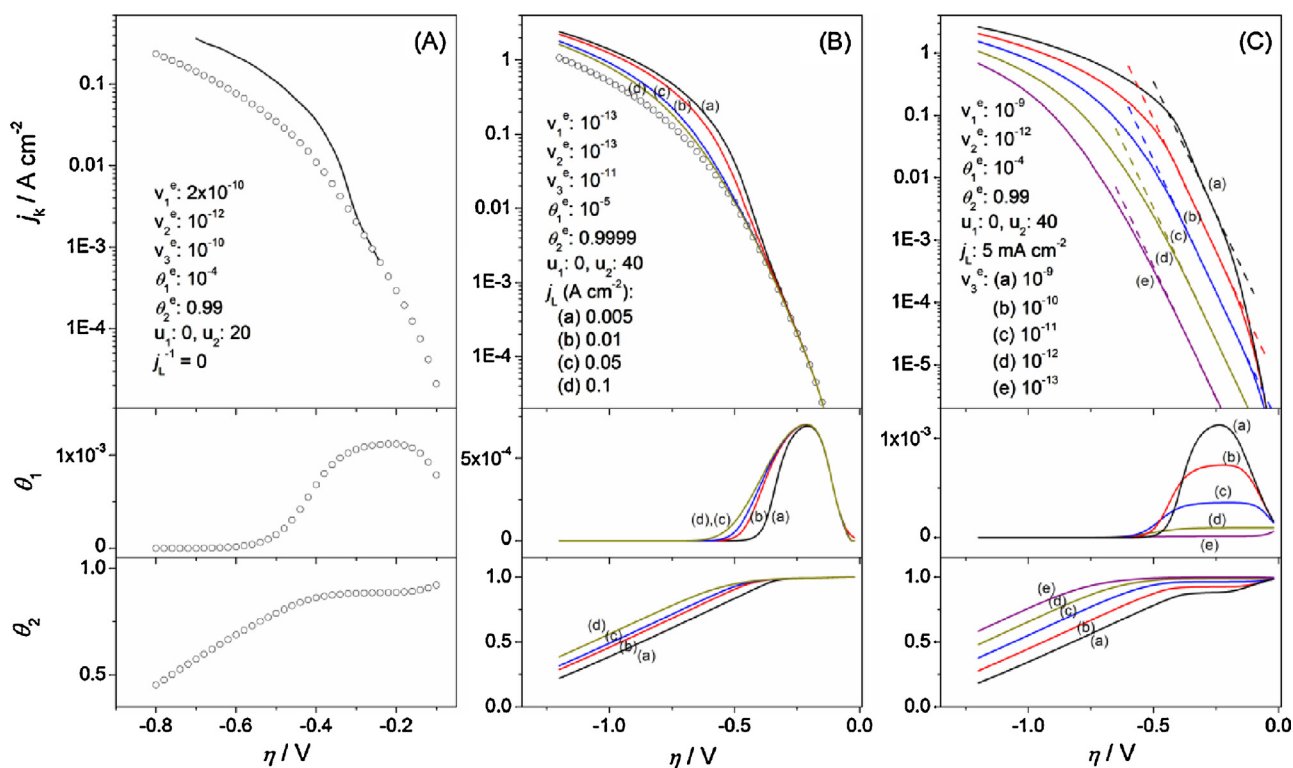
Fig. 6. (A) $j_k(\eta)$ dependence calculated from linear fittings of $j^{-1}(j_L^{-1})$ plots in Fig. 5B (solid line). Open symbols are the activated $j_{act}(\eta)$ and $\theta_i^*(\eta)$ responses calculated with Eq. (14). (B) $j_k(\eta)$ and $\theta_i(\eta)$ dependencies calculated with Eq. (15) for varying values of j_L (solid lines). The activated $j_{act}(\eta)$ response calculated with Eq. (14) is included (open symbols). (C) $j_k(\eta)$ and $\theta_i(\eta)$ dependencies calculated with Eq. (15) (solid lines) for varying values of v_3^e (v_i^e in mol s^{-1} cm^{-2}). Dashed lines are linear fittings of $j_k(\eta)$ dependencies over apparently linear regions with a Tafel slope of 0.118 V dec^{-1}.
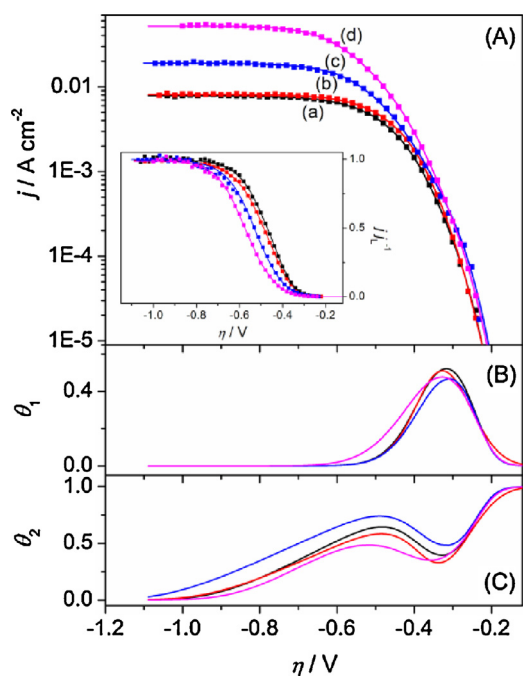
Fig. 7. Experimental $j(\eta)$ curves measured on Pt disk microelectrodes (symbols) and their correlations with Eq. (12) (solid lines) (A), and corresponding simulated $\theta_1(\eta)$ (B) and $\theta_2(\eta)$ (C) dependencies. j_L (mA cm^{-2})/r (μm) = 7.9 /12.5 (a), 8.1/12.0 (b), 19.0/5.2 (c), 52.7/1.9 (d). Parameters are listed in Table 1. Inset graph in (A) shows the experimental and theoretical $j(\eta)$ curves normalized with respect to j_L.

not match the real activated response $j_{act}(\eta)$ over the entire potential range, as can be seen in the example shown in Fig. 6B. Only at the lower overpotentials where the mass transport effects are negligibly j_k tends to approach the j_{act} values. Moreover, it was frequently reported the existence of an apparently linear region with a Tafel slope of 118 V dec^{-1} in the logarithmic $j_k(\eta)$ dependencies. This Tafel slope can be obtained from the Direct Route for certain domains of values of the kinetic parameters, for example those shown in Fig. 6C. From these curves it is verified that a linear region in the $j_k(\eta)$ dependence is set on an overpotential range where the coverages of both adsorbed intermediates reach almost constant (but not necessarily null) values. The extension of this overpotential range depends on the relative values of v_2^e and v_3^e (the electrochemical steps), but the exchange current density that is obtained from extrapolation of this linear region to $\eta = 0$ (j^0) is affected by many parameters, so j^0 cannot be associated exclusively to the rate constant of a particular step.

4.3. Fitting of experimental j(η) data

Steady state $j(\eta)$ curves measured on Pt disk microelectrodes of different radii (12.5 $\geq r(\mu m) > 1$) were correlated using Eq. (12). The values of j_L were calculated with the radii (estimated as indicated in the Experimental Section) using the well known $j_L(r)$ dependence for a disk microelectrode [35] $j_L = (4/\pi)$ 4$FDO_2C^*_{O2}/r$, and adopting 1.12×10^{-5} mol cm^{-3} and 1.8×10^{-5} cm^2 s^{-1} for the solubility and diffusion coefficient of dissolved oxygen [2], respectively. As can be seen in Fig. 7A, the quality of all the fittings was quite good over the whole analyzed potential interval. The resulting kinetic parameters are listed in Table 1. Even when the data came from different electrodes with j_L dispersed over a range of values covering a variation of about one order of magnitude, the correlations led to kinetic parameters with little dispersion and that followed the same trend in all electrodes ($v_3^e \gg v_2^e > v_1^e, \theta_2^e \to 1, \theta_1^e \to 0, u_2 \gg u_1$). These values are critically analyzed below. Moreover, the simulated $\theta_1(\eta)$ and $\theta_2(\eta)$ dependencies that resulted with the calculated parameters are shown in Figs. 7B and C, respectively.

The coverage of OH$_{ad}$ at the *orr* equilibrium potential resulted very close to 1, which contrasts with the expected almost null value that should result due to the electro-oxidation of OH$_{ad}$ at such anodic potentials [36,37]. Consequently, the fraction of free available sites is almost null ($1 - \theta^e \to 0$) and the equilibrium coverage of O$_{ad}$ results very small, which is also opposite to what should be expected considering studies of the Pt anodic behavior in O$_2$-free solutions [37]. In fact, it is known that the electro-oxidation of Pt is a rather complex process that involves irreversible changes of the electro-adsorbed species [38–40] leading to undefined PtOO-based surface compounds. Then, the Direct Route model, which considers only two adsorbed oxygenated species (O$_{ad}$ and OH$_{ad}$), is not realistic at potentials close to the *orr* equilibrium potential. Thus, it is likely that the large OH$_{ad}$ coverages that resulted from the experimental $j(\eta)$ correlations with the Direct Route is a fictitious situation caused by the inability of this simple mechanism to take into account the transformation of OH$_{ad}$ into site-inhibiting species. As the O$_{ad}$ coverage is conditioned by the concentration of dissolved oxygen through step 1, the only way that the model finds to correlate the $j(\eta)$ dependences at low η is to increase the θ_2^e values to near unity. Thus, the obtained high θ_2^e values are not realistic and represent in fact a surface almost fully covered by oxidized and irreversibly adsorbed species of undefined nature at the *orr* equilibrium potential. These limitations in the model also affect the Frumkin interaction parameters, which resulted unusually large (particularly u_2, which value was around 20 while the reported value measured on single crystals is about 5 [41]) having strong effects in the $j(\eta)$ curve. However, such large u_2 values, and particularly their differences with u_1, could also be

Table 1

Kinetic parameters of the *orr* operating through the Direct Route that resulted from correlations of $j(\eta)$ curves measured on Pt with Eq. (12). v_i^e in mol s^{-1} cm^{-2}, u_i in RT units, $\alpha = \lambda = 0.5$. j_{max} values were calculated with Eq. (13).
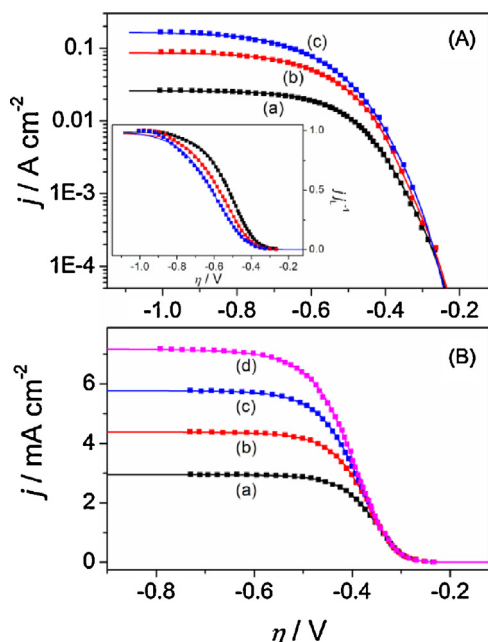
Data		j_L A cm^{-2}	v_1^e	v_2^e	v_3^e	θ_1^e	θ_2^e	u_1	u_2	j_{max} A cm^{-2}
Fig. 7A	(a)	0.0079	1.2×10^{-18}	2.0×10^{-16}	2.2×10^{-11}	9.6×10^{-5}	0.99990	3.2	17.4	0.00781
	(b)	0.0081	3.5×10^{-17}	1.3×10^{-16}	9.7×10^{-11}	9.6×10^{-5}	0.99986	5.9	20.9	0.00807
	(c)	0.0190	3.2×10^{-18}	6.0×10^{-16}	2.5×10^{-11}	9.8×10^{-5}	0.99990	1.9	20.5	0.0188
	(d)	0.0527	2.9×10^{-18}	1.1×10^{-15}	1.3×10^{-10}	2.4×10^{-4}	0.99975	5.8	14.6	0.0520
Fig. 8A	(a)	0.0264	4.5×10^{-18}	6.1×10^{-16}	3.2×10^{-11}	9.9×10^{-5}	0.99990	2.2	19.8	0.02636
	(b)	0.0887	6.1×10^{-18}	8.5×10^{-16}	2.0×10^{-10}	1.5×10^{-4}	0.999849	3.1	19.2	0.08855
	(c)	0.1667	3.4×10^{-18}	5.4×10^{-16}	5.4×10^{-11}	2.0×10^{-5}	0.999979	3.3	26.8	0.16592
Fig. 8B	(a)	0.00295	4.3×10^{-19}	9.2×10^{-17}	1.1×10^{-10}	5.9×10^{-6}	0.999992	5.2	15.1	0.00295
	(b)	0.00438	2.2×10^{-19}	1.9×10^{-16}	1.1×10^{-10}	5.7×10^{-6}	0.999993	4.1	14.6	0.00437
	(c)	0.00578	3.5×10^{-19}	9.8×10^{-17}	6.9×10^{-11}	2.2×10^{-6}	0.999997	6.8	30.3	0.00578
	(d)	0.00718	1.4×10^{-19}	4.2×10^{-16}	4.2×10^{-11}	1.0×10^{-5}	0.999989	4.8	26.3	0.00717

Fig. 8. Reported experimental $j(\eta)$ dependencies (symbols) and respective correlations using Eq. (12) (solid lines). (A) Electrodeposited Pt hemispherical microelectrodes [2], $r(\mu m) = 3.6$ (a), 1.08 (b), 0.57 (c). (B) Polycrystalline Pt RDE [42], ω (rpm) = 400 (a), 900 (b), 1600 (c), 2500 (d). Parameters are listed in Table 1. Inset graph in (A) shows the experimental and theoretical $j(\eta)$ dependencies normalized with respect to j_L.

indicative of strong lateral interactions between intermediates [23]. Moreover, in spite of the low value of v_1^e, the calculated j_{max} magnitudes (also listed in Table 1) result almost identical to j_L due to the near complete coverage of adsorbed intermediates at the equilibrium potential ($\theta^e \cong 1$) and the relatively large values of u_1. In addition, v_2^e is about five orders of magnitude smaller than v_3^e, so that step 2 controls the variations of the coverages at large η and the potential shift of the $j(\eta)$ curve. For these kinetic parameters, the coverage of OH$_{ad}$ decreases upon η increases allowing a proportional increment of the O$_{ad}$ coverage.

To subject the model to a more extensive test, it was also contrasted with published data. Thus, Eq. (12) was used to correlate reported $j(\eta)$ curves measured for the *orr* on electro-deposited Pt hemispheric microelectrodes [2] and on a polycrystalline Pt RDE [42]. The correlations are shown in Fig. 8A (microelectrodes) and 8B (RDE), and the resulting parameters are listed in Table 1. In all cases the fitting quality was good, and the calculated kinetic parameters follow the same trend and have values that are reasonably close (taking into account the different sources) to those obtained from Fig. 7.

5. CONCLUSIONS

A complete analysis of the *orr* operating in steady state through the Direct Route, in conjunction with proper models for the behavior of the adsorbed intermediates (Frumkin isotherm) and for the mass transport of dissolved oxygen was presented. This analysis leaded to a set of equations that permitted to obtain the dependencies of the current density and coverages of adsorbed intermediates (O$_{ad}$ and OH$_{ad}$) on the overpotential in terms of the kinetic parameters of the elementary steps and adsorption parameters. An exploration of the descriptive capabilities carried out by simulations over wide ranges of these kinetic and adsorption parameters allowed to understand the effects of these

parameters on different features of the $j(\eta)$ dependencies. One of these features is the maximum current density (j_{max}), which may be quite different to the limiting current density (j_L) or may approach to it, depending on the rate of oxygen adsorption, the j_L value, and the adsorption parameters. Besides, the potential shifts of the $j(\eta)$ dependencies are mostly dominated by the relative values of the rate constants of the electrochemical steps, and their slopes are strongly affected by the difference between the Frumkin interaction parameters of OH$_{ad}$ and O$_{ad}$ caused by lateral interactions.

The application of Tafel plots calculated from the Koutecký–Levich method, which is the usual and widely accepted method to separate the kinetic current density (j_k) from the $j(\eta)$ dependence, was critically analyzed. It was shown that when the Direct Route operates, j_k obtained through the KL method is not totally free of mass transport effects and do not correspond to the real activated current density. Besides, the $j_k(\eta)$ dependencies may present linear regions with Tafel slopes similar to those reported for Pt (i.e. 118 mV dec^{-1}) over certain range of η where the coverages of intermediates remain almost invariant, although the exchange current density calculated from extrapolation of this linear region is not representative of any elementary step. These evidences show that the kinetic analysis of the *orr* through Tafel plots obtained from the KL method could be misleading, even when the reaction operates through the simplest possible mechanism (as it is the Direct Route).

The theoretical equations that resulted from the Direct Route were applied to correlate experimental $j(\eta)$ curves both measured in this work on Pt disk microelectrodes, and taken from reported data (Pt hemispherical microelectrodes [2] and a rotating disk electrode [42]). The quality of the correlations was good in all cases and the obtained kinetic parameters showed little dispersion. However, the model clearly fails the representation of the processes at low overpotentials (anodic potentials close to the *orr* equilibrium potential) where the electro-oxidation of OH$_{ad}$ and O$_{ad}$ to irreversibly adsorbed oxygen-based species is expected. On that sense, the obtained parameters indicate an almost complete coverage of OH$_{ad}$ at the *orr* equilibrium potential that remains down to overpotentials of -0.2 V, which in fact is a falsity generated by the model to account for the transformation of intermediates into oxidized site blocking species at anodic potentials. Besides, the correlations led to values of j_{max} almost identical to j_L, and a slow conversion of O$_{ad}$ into OH$_{ad}$ at intermediate overpotentials that is strongly affected by lateral interactions. Thus, in spite that the Direct Route is only a partial representation of the complete *orr* mechanism, it is capable to reproduce experimental $j(\eta)$ dependencies measured on Pt electrodes with different configurations. In order to gain real physical meaning on the full set of kinetic parameters, it should be incorporated to this mechanistic model a more complete representation of the electro-oxidation of the active sites into oxygen-based spectator species. A similar analysis of other dependencies commonly used for the evaluation of reaction mechanisms (such as the reaction orders respect to proton concentration and oxygen partial pressure) that result from the Direct Route would provide additional support in favor or against its prevalence in the *orr* on the different metal electrodes, and will be the subject of future communications.

References

[1] J.X. Wang, N.M. Markovic, R.R. Adzic, Kinetic analysis of oxygen reduction on Pt (111) in acid solutions: Intrinsic kinetic parameters and anion adsorption effects, J. Phys. Chem. B 108 (2004) 4127–4133.

[2] S. Chen, A. Kucernak, Electrocatalysis under conditions of high mass transport rate: Oxygen reduction on single submicrometer-sized Pt particles supported on carbon, J. Phys. Chem. B 108 (2004) 3262–3276.

[3] V.P. Zhdanov, B. Kasemo, Kinetics of electrochemical O_2 reduction on Pt, Electrochem. Commun. 8 (2006) 1132–1136.

[4] W.E. Mustain, J. Prakash, A model for the electroreduction of molecular oxygen, J. Electrochem. Soc. 154 (2007) A668–A676.

[5] J.X. Wang, J. Zhang, R.R. Adzic, Double-trap kinetic equation for the oxygen reduction reaction on Pt(111) in acidic media, J. Phys. Chem. A 111 (2007) 12702–12710.

[6] S. Gottesfeld, Some observations on the oxygen reduction reaction (ORR) at platinum catalysts based on post year 2000 reports, ECS Trans 6 (2008) 51–67.

[7] S. Strbac, The effect of pH on oxygen and hydrogen peroxide reduction on polycrystalline Pt electrode, Electrochim. Acta 56 (2011) 1597–1604.

[8] P.S. Ruvinskiy, A. Bonnefont, C. Pham-Huu, E.R. Savinova, Using ordered carbon nanomaterials for shedding light on the mechanism of the cathodic oxygen reduction reaction, Langmuir 27 (2011) 9018–9027.

[9] A. Kriston, B.B. Berkes, P.L. Simon, G. Inzelt, K. Dobos, A. Nemes, Unusual surface mass changes in the course of the oxygen reduction reaction on platinum and their explanation by using a kinetic model, J.Solid State Electrochem. 16 (2012) 1723–1732.

[10] N.P. Subramanian, T.A. Greszler, J. Zhang, W. Gu, R. Makharia, Pt-oxide coverage-dependent oxygen reduction reaction (ORR) kinetics, J. Electrochem. Soc. 159 (2012) B531–B540.

[11] M. Moore, A. Putz, M. Secanell, Investigation of the ORR using the double-trap intrinsic kinetic model, J. Electrochem. Soc. 160 (2013) F670–F681.

[12] A.M. Gómez-Marín, J.M. Feliu, New insights into the oxygen reduction reaction mechanism on Pt(111): A detailed electrochemical study, ChemSusChem 6 (2013) 1–11.

[13] M. Rouhet, S. Bozdech, A. Bonnefont, E.R. Savinova, Influence of the proton transport on the ORR kinetics and on the H_2O_2 escape in three-dimensionally ordered electrodes, Electrochem. Commun. 33 (2013) 111–114.

[14] K. Kinoshita, Electrochemical Oxygen Technology, John Wiley & Sons, New York, 1992.

[15] I. Katsounaros, W.B. Schneider, J.C. Meier, U. Benedikt, P.U. Biedermann, A.A. Auer, K.J.J. Mayrhofer, Hydrogen peroxide electrochemistry on platinum: towards understanding the oxygen reduction reaction mechanism, Phys. Chem. Chem. Phys. 14 (2012) 7384–7391.

[16] H.S. Wroblowa, Yen-Chi-Pan, G. Razumney, Electroreduction of oxygen. A new mechanistic criterion, J. Electroanal. Chem. 69 (1976) 195–201.

[17] E. Yeager, Recent advances in the science of electrocatalysis, J. Electrochem. Soc. 128 (1981) 160C–171C.

[18] J.K. Norskov, J. Rossmeisl, A. Logadottir, L. Lindqvist, J.R. Kitchin, T. Bligaard, H. Jónsson, Origin of the overpotential for oxygen reduction at a fuel-cell cathode, J. Phys. Chem. B 108 (2004) 17886–17892.

[19] A. Panchenko, M.T.M. Koper, T.E. Shubina, S.J. Mitchell, Ab initio calculations of intermediates of oxygen reduction on low-index platinum surfaces, J. Electrochem. Soc. 151 (2004) A2016–A2027.

[20] J. Koutecký, V.G. Levich, The use of a rotating disk electrode in the studies of electrochemical kinetics and electrolytic processes, Zh. Fiz. Khim. 32 (1958) 1565–1575.

[21] A.J. Bard, L.R. Faulkner, Electrochemical methods. Fundamentals and applications, 2nd Ed., John Wiley & Sons, New York, 2001, pp. 341 Chapter 9.

[22] A.J. Bard, L.R. Faulkner, Electrochemical methods. Fundamentals and applications, 2nd Ed., John Wiley & Sons, New York, 2001, pp. 90 Chapter 3.

[23] E. Gileadi, Electrode kinetics for chemists, chemical engineers, and materials scientists, VCH, New York, 1993, pp. 266 Chapter 1.

[24] S. Chen, A. Kucernak, Electrocatalysis under conditions of high mass transport: Investigation of hydrogen oxidation on single submicron Pt particles supported on carbon, J. Phys. Chem. B 108 (2004) 13984–13994.

[25] M.D. Arce, J.L. Fernández, M.R. Gennero de Chialvo, A.C. Chialvo, Fabrication, characterization and application of graphite ring ultramicroelectrodes for kinetic studies of fuel cell reactions under high mass-transport rates, J. Electroanal. Chem. 642 (2010) 41–51.

[26] M.D. Arce, H.L. Bonazza, J.L. Fernández, Kinetic analysis of the hydrogen electrode reaction in unbuffered media. Theory and studies on Pt microelectrodes, Electrochim. Acta 107 (2013) 248–260.

[27] F.F. Fan, J.L. Fernández, B. Liu, J. Mauzeroll, C.G. Zoski, Handbook of Electrochemistry, in: G.G. Zoski (Ed.), Elsevier, Amsterdam, 2007, pp. 189 Chapter 6.

[28] P.M. Quaino, M.R. Gennero de Chialvo, A.C. Chialvo, Hydrogen electrode reaction: A complete kinetic description, Electrochim. Acta 52 (2007) 7396–7403.

[29] R. Woods, Hydrogen adsorption on platinum, iridium and rhodium electrodes at reduced temperatures and the determination of real surface area, J. Electroanal. Chem. 49 (1974) 217–226.

[30] J.L. Fernández, D.A. Walsh, A.J. Bard, Thermodynamic guidelines for the design of bimetallic catalysts for oxygen electroreduction and rapid screening by scanning electrochemical microscopy. M-Co (M: Pd, Ag, Au), J. Am. Chem. Soc. 127 (2005) 357–365.

[31] M.A. Genshaw, A. Damjanovic, J.O'.M. Bockris, Hydrogen peroxide formation in oxygen reduction at gold electrodes. I. Acid solutions, J. Electroanal. Chem. 15 (1967) 163–172.

[32] R.R. Adzic, S. Strbac, N. Anastasijevic, Electrocatalysis of oxygen on single crystal gold electrodes, Mater. Chem. Phys. 22 (1989) 349–375.

[33] B. Liu, A.J. Bard, Scanning electrochemical microscopy. 45. Study of the kinetics of oxygen reduction on platinum with potential programming of the tip, J. Phys. Chem. B 106 (2002) 12801–12806.

[34] K.-L. Hsueh, D.-T. Chin, S. Srinivasan, Electrode kinetics of oxygen reduction. A theoretical and experimental analysis of the rotating ring-disk electrode method, J. Electroanal. Chem. 153 (1983) 79–95.

[35] A.J. Bard, L.R. Faulkner, Electrochemical methods. Fundamentals and applications, 2nd Ed., John Wiley & Sons, New York, 2001, pp. 176 Chapter 5.

[36] S.G. Rinaldo, W. Lee, J. Stumper, M. Eikerling, Mechanistic principles of platinum oxide formation and reduction, Electrocatal. 5 (2014) 262–272.

[37] M. Wakisaka, H. Suzuki, S. Mitsui, H. Uchida, M. Watanabe, Identification and quantification of oxygen species adsorbed on Pt(111) single-crystal and polycrystalline Pt electrodes by photoelectron spectroscopy, Langmuir 25 (2009) 1897–1900.

[38] B.E. Conway, B. Barnett, H. Angerstein-Kozlowska, B.V. Tilak, A surface electrochemical basis for the direct logarithmic growth law for initial stages of extension of anodic oxide films formed at noble metals, J. Chem. Phys. 93 (1990) 8361–8373.

[39] L.D. Burke, D.T. Buckley, The complex nature of hydrous oxide film behavior on platinum, J. Electroanal. Chem. 405 (1996) 101–109.

[40] G. Jerkiewicz, G. Vatankhah, J. Lessard, M.P. Soriaga, Y.-S. Park, Surface-oxide growth at platinum electrodes in aqueous H_2SO_4. Reexamination of its mechanism through combined cyclic-voltammetry electrochemical quartz-crystal nanobalance, and Auger electron spectroscopy measurements, Electrochim. Acta 49 (2004) 1451–1459.

[41] A. Burná, V. Climent, J.M. Feliu, New understanding of the nature of OH adsorption on Pt(111) electrodes, Electrochem. Commun. 9 (2007) 2789–2794.

[42] U.A. Paulus, A. Wokaun, G.G. Scherer, T.J. Schmidt, V. Stamenkovic, N.M. Markovic, P.N. Ross, Oxygen reduction on high surface area Pt-based alloy catalysts in comparison to well defined smooth bulk alloy electrodes, Electrochim. Acta 47 (2002) 3787–3789.